Electronic Supplementary Information

Crafting Double Perovskites/Hollow Conjugated Microporous Polymer Heterostructure for Dual-Channel H_2O_2 Production

Jian Yi[a], Jianfei Chen[b], Xue Li[a,*] and Tao Cai[a,*]

[a]College of Chemistry and Molecular Sciences, State Key Laboratory of Power Grid Environmental Protection, Wuhan University, Wuhan, Hubei 430072, P. R. China

[b]School of Electrical Engineering and Automation, State Key Laboratory of Power Grid Environmental Protection, Wuhan University, Wuhan, Hubei 430072, P. R. China

*To whom correspondence should be addressed.
Email address: chemcaitao@whu.edu.cn (T. Cai)
li.x@whu.edu.cn (X. Li)

Experiment Section

Materials

All chemicals were obtained from commercial sources and used as received unless otherwise noted. 5,10,15,20-Tetra(4-ethynylphenyl)-21*H*,23*H*-porphyrin (Pr, ≥97%) and 1,2,4,5-tetrafluoro-3,6-diiodobenzene (Fb, >98%) were purchased from Jilin Chinese Academy of Sciences Yanshen Technology. Ammonium hydroxide solution (28.0~30.0 wt% NH_3 basis), tetraethyl orthosilicate (TEOS, 98%), triethylamine (TEA, ≥99.5%), tetrakis(triphenylphosphine)palladium(0) ($Pd(PPh_3)_4$, 99%) and cuprous iodide (CuI, 98%) were purchased from Sigma Aldrich. Cesium bromide (CsBr, 99.5%), silver bromide (AgBr, 98%), bismuth bromide ($BiBr_3$, 98%), potassium iodide (KI, 99%) and potassium biphthalate (99.8%) were purchased from Macklin.

Instrumentation

Nuclear Magnetic Resonance (NMR): Solid-state ^{13}C cross-polarization/magic angle spinning nuclear magnetic resonance (^{13}C CP/MAS NMR) spectra were recorded on a Bruker AVANCE III 400 WB spectrometer operating at 100.62 MHz for ^{13}C with a 4 mm MAS NMR probe, spinning at 10 kHz.

Field Emission Scanning Electron Microscopy (FESEM): The morphology of the samples was observed by FESEM (JEOL-6700F, JEOL Ltd., Japan) operating at an accelerating voltage ranging from 0.1 to 20 kV.

Transmission Electron Microscopy (TEM): The morphology and size of the samples were analyzed by TEM (JEOL-2010, JEOL Ltd., Japan) operating at an accelerating voltage of 200 kV.

X-Ray Diffraction (XRD): Powder XRD patterns were obtained on a Rigaku Smartlab with Cu Kα line (λ = 1.5418 Å).

Thermogravimetric Analysis (TGA): The thermal stability was investigated by TGA. The samples were heated from 30 ºC to around 1000 ºC with a heating rate of 10 ºC min^{-1} under a dry nitrogen atmosphere in a thermal analyzer (TGS-II, Perkin-Elmer).

Fourier Transform Infrared Spectroscopy (FTIR): FTIR analysis of the samples was conducted on a NICOLET 5700 FTIR spectrophotometer. Each spectrum was collected by cumulating 64 scans.

Specific Surface Area Analyzer: The N_2 absorption-desorption isotherms were collected by AUTOSORB-1 Analyzer from Quantachrome Instruments and the specific surface area was acquired by the Brunauer-Emmett-Teller (BET) method, while the pore size distribution was calculated from the desorption branch according to the BJH model.

X-Ray Photoelectron Spectroscopy (XPS): Surface composition of the samples was investigated by XPS on a Kratos AXIS Ultra DLD spectrometer sourcing with a monochromatized Al Kα X-ray source (1468.71 eV photons).

Optical Spectrophotometer: Ultraviolet-visible diffuse reflectance (UV-vis DR) spectra were measured by UV-visible spectrophotometer (UV-vis, UV3600, Shimadzu).

Photoluminescence (PL) Spectrophotometer: The PL emission spectra were recorded on a PerkinElmer LS 55 Fluorescence spectrometer and the time-resolved photoluminescence emission decay spectra (TRPL) were recorded on a Multifunctional Fluorescence Imaging System (FLM300).

Electron Paramagnetic Resonance (EPR): A JEOL JES X320 spectrometer in conjunction with a split-coil 6T superconducting magnet was used for X-band (10.0 GHz) electron paramagnetic resonance.

Electrochemical Workstation: Electrochemical measurements were executed on a Metrohm Autolab PGSTAT302N in a three-electrode electrochemical cell equipped with an electrochemical station. First, photocatalyst (6 mg) was dispersed in Nafion (3 mL, 0.2 wt%) by the ultrasonic instrument. Then the samples were dripped on ITO coated glasses which were places on top of a glassy carbon as the working electrode, and the samples were dried under infrared irradiation. With Na_2SO_4 aqueous solution (0.1 M) supplied as the electrode, the Ag/AgCl as the reference electrode and the platinum wire as the counter electrode. Meanwhile, 300 W Xe lamp placed at 2 cm away from the photoelectrochemical cell were employed as the light source.

The photocurrents were tested under 300 W Xe lamp with light on-off cycles at a time interval of 30 s and the scan rate was 100 mV s^{-1}. The Mott-Schottky measurement was performed at frequencies of 500 Hz, 1000 Hz and 1500 Hz in dark conditions. The electrochemical impedance spectroscopy (EIS) was carried out at a bias potential of +0.5 V in the dark.

Rotating Disk Electrode (RDE) Measurements: The number of electrons transferred during the oxygen reduction reaction (ORR) was evaluated using a CHI660E electrochemical workstation with a three-electrode system. The working electrode was prepared by dispersing 2.0 mg of catalyst in 1 mL ethanol and 10 μL Nafion solution, sonicating for 30 min, and drop-casting 6 μL onto a polished rotating disk electrode (RDE), dried under an infrared lamp. Linear sweep voltammograms were recorded in O_2-saturated 0.1 M phosphate buffer solution (PBS, pH 7) at 10 mV s^{-1} with varying rotation speeds, using a platinum wire counter electrode and an Ag/AgCl reference electrode. The average number of electrons (n) was calculated using the Koutecky-Levich equation:

$$1/J = 1/J_L + 1/J_K = 1/B\omega^{1/2} + 1/J_K$$

$$B = 0.62\ nFC_0D_0^{2/3}\nu^{1/6}$$

where J is the measured current density, J_K and J_L are the kinetic and diffusion-limiting current densities, ω is the angular velocity (rad s^{-1}), n is the electron transfer number, F is the Faraday constant (96485 C mol^{-1}), C_0 is the O_2 bulk concentration (1.26×10^{-6} mol cm^{-3}), D_0 is the O_2 diffusion coefficient (2.7×10^{-5} cm^2 s^{-1}), and ν is the kinematic viscosity of electrolyte (0.01 cm^2 s^{-1}).

Apparent Quantum Efficiency (AQE) Measurement: The AQE was measured using a 300 W Xe lamp with optical filters at different wavelengths. Light intensity was averaged at five points using an optical meter. Then, AQE was calculated as:

$$AQE(\%) = 2CN_A/(SIt\lambda/hc) \times 100\% = 2CN_Ahc/SIt\lambda \times 100\%$$

where I is the light intensity (W m^{-2}), S is the irradiation area (m^2), t is the irradiation time (s), λ is the monochromatic light wavelength (m), h is the Planck constant (6.626×10^{-34} m^2 kg s^{-1}), and c is the speed of light (3.0×10^8 m s^{-1}).

Density Functional Theory (DFT) Calculations: Density functional theory as implemented in the Vienna Ab-initio Simulation Package (VASP)[1,2] was employed to optimize geometry structures. The exchange-correlation interactions were described by the generalized gradient approximation (GGA) in the form of the Perdew-Burke-Ernzerhof functional (PBE).[3] We have chosen the projected augmented wave (PAW) potentials[4,5] to describe the ionic cores and take valence electrons into account using a plane wave basis set with a kinetic energy cutoff of 350 eV. The electronic energy was considered self-consistent when the energy change was smaller than 10^{-6} eV and in the atomic structural relaxation, all the internal degrees of freedom are allowed to relax until the Hellmann-Feynman force on each atom is less than 0.01 eV/Å. The Brillouin-zone integration was sampled with a Monkhorst-Pack mesh of 12 × 12 × 12 in the structural relaxation calculations.[6] In addition, the electronic structures are calculated with SOC.[7] The topological edge states are calculated from the maximally localized Wannier basis as implemented in the Wannier90 and WannierTools packages.[8,9]

Synthesis of *h*PrFb[10-15]

Typically, TEOS (9.0 mL) was added dropwise to a mixture of ethanol (150 mL), ultrapure water (15 mL) and ammonium hydroxide solution (3.0 mL, 28-30 wt% NH_3 basis). The mixture was stirred vigorously at room temperature for 12 h. Finally, the raw product was purified by five cycles of centrifugation/redispersion/washing in excessive ethanol and ultrapure water. The SiO_2 microspheres were centrifuged and stored in ethanol prior to use.

The SiO_2 (240 mg) were dispersed in a mixture of toluene (15 mL) and TEA (15 mL). Pr (85.3 mg, 0.12 mmol), Fb (96.4 mg, 0.24 mmol), $Pd(PPh_3)_4$ (13.9 mg) and CuI (2.3 mg) were added in sequence. The reaction mixture was purged with argon for 20 min to remove dissolved oxygen. The reaction was allowed to proceed at 90 ºC for 48 h. Following this, the reaction was halted by cooling the Schlenk tube into an icy water bath. The crude product was collected by centrifugation and washed with dichloromethane, acetone and methanol thrice. After Soxhlet extraction with THF for 24 h, the SiO_2@PrFb were dried under vacuum at 80 ºC for 24 h and obtained as a purple powder.

The SiO_2@PrFb (300 mg) were added to an aqueous HF solution (5 mL, 20 wt%). The etching process was allowed to proceed at room temperature overnight. Afterwards, the crude products were subjected to a purification process consisting of five cycles of centrifugation, redispersion and washing in excessive water/ethanol mixed solution to eliminate any residual HF and SiF_4. Finally, the *h*PrFb was collected by centrifugation and dried under vacuum at 80 ºC for 12 h to yield a purple powder.

Synthesis of CABB@*h*PrFb

The incorporation of perovskite nanocrystals into the hollow conjugated microporous polymers was achieved by improving methods from a previously reported protocol.[16] CsBr (42.6 mg, 0.2 mmol), AgBr (18.8 mg, 0.1 mmol) and $BiBr_3$ (44.9 mg, 0.1 mmol) were sequentially added to DMSO (5 mL). The reaction mixture was sonicated to dissolve the solids and form the precursor solution. The precursor solution was then evenly distributed into ten aliquots, each containing 0.5 mL. Different amounts of *h*PrFb (1, 2, 4 and 8 mg) were added to one aliquot and stirred vigorously at room temperature for 1 h. The reaction mixture was then transferred to isopropanol (5 mL) and stirred for an additional 15 min. The crude products were purified through three cycles of centrifugation, redispersion and washing with excess isopropanol. Finally, the CABB@*h*PrFb-X were collected by centrifugation and dried under vacuum at 60 ºC for 12 h, yielding a purple powder. Based on the amount of *h*PrFb added, the products were labeled as CABB@*h*PrFb-X (where X = 1, 2, 4 and 8, corresponding to the amount of *h*PrFb added).

Assessment of Photocatalytic Performance

The CABB@*h*PrFb (5.0 mg) was dispersed in 40 mL deionized water in a 100 mL tubular quartz reactor. Pure oxygen was bubbled through the solution for 10 min, and the mixture was kept in the dark to achieve adsorption equilibrium at room temperature. Irradiation was carried out using 300 W Xe lamp (PLSSXE300, Perfect Light Company, Beijing, China). At designated time intervals, aliquots of the solution were collected, centrifuged, and filtered through a 0.22 μm membrane to remove particulate matter. The concentration of H_2O_2 was quantified using an iodometric method based on a previously

reported procedure.[17] Briefly, 1.0 mL of the sample was added to a mixture of KI (0.4 M, 1.0 mL) and potassium biphthalate (0.1 M, 1.0 mL). After allowing the reaction to proceed for 30 min, H_2O_2 oxidized I^- to I_3^- under acidic conditions. The I_3^- complex exhibited a strong absorption peak around 350 nm in UV-vis spectroscopy, enabling the quantification of the total H_2O_2 produced over the course of the reaction. The pure $Cs_2AgBiBr_6$ perovskites and *h*PrFb served as a reference material for comparison. To evaluate the reproducibility and stability of the sample during the photocatalytic H_2O_2 generation, eight consecutive photocatalytic cycles were performed with the same catalyst. After each cycle, the catalyst was separated by centrifugation, recovered from the centrifuge tube, and placed into a beaker with fresh solution. The suspension was magnetically stirred in the dark before being exposed to visible light irradiation for the subsequent cycle. To further assess the stability, the catalyst was filtered, dried and analyzed by XRD, TEM and XPS after eight reaction cycles.

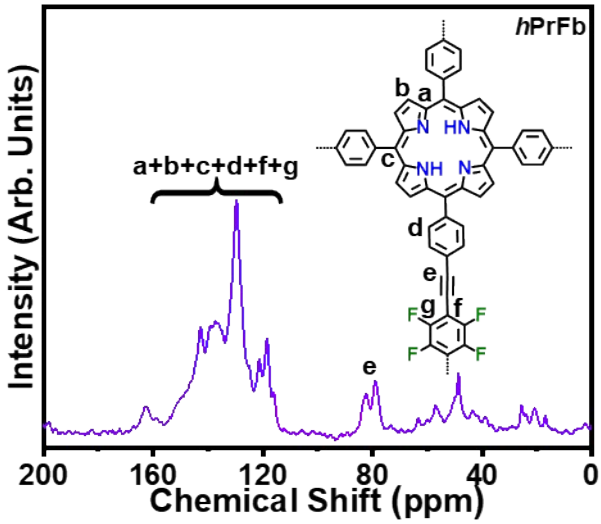

Fig. S1 Solid state ^{13}C CP/MAS NMR spectrum of *h*PrFb.

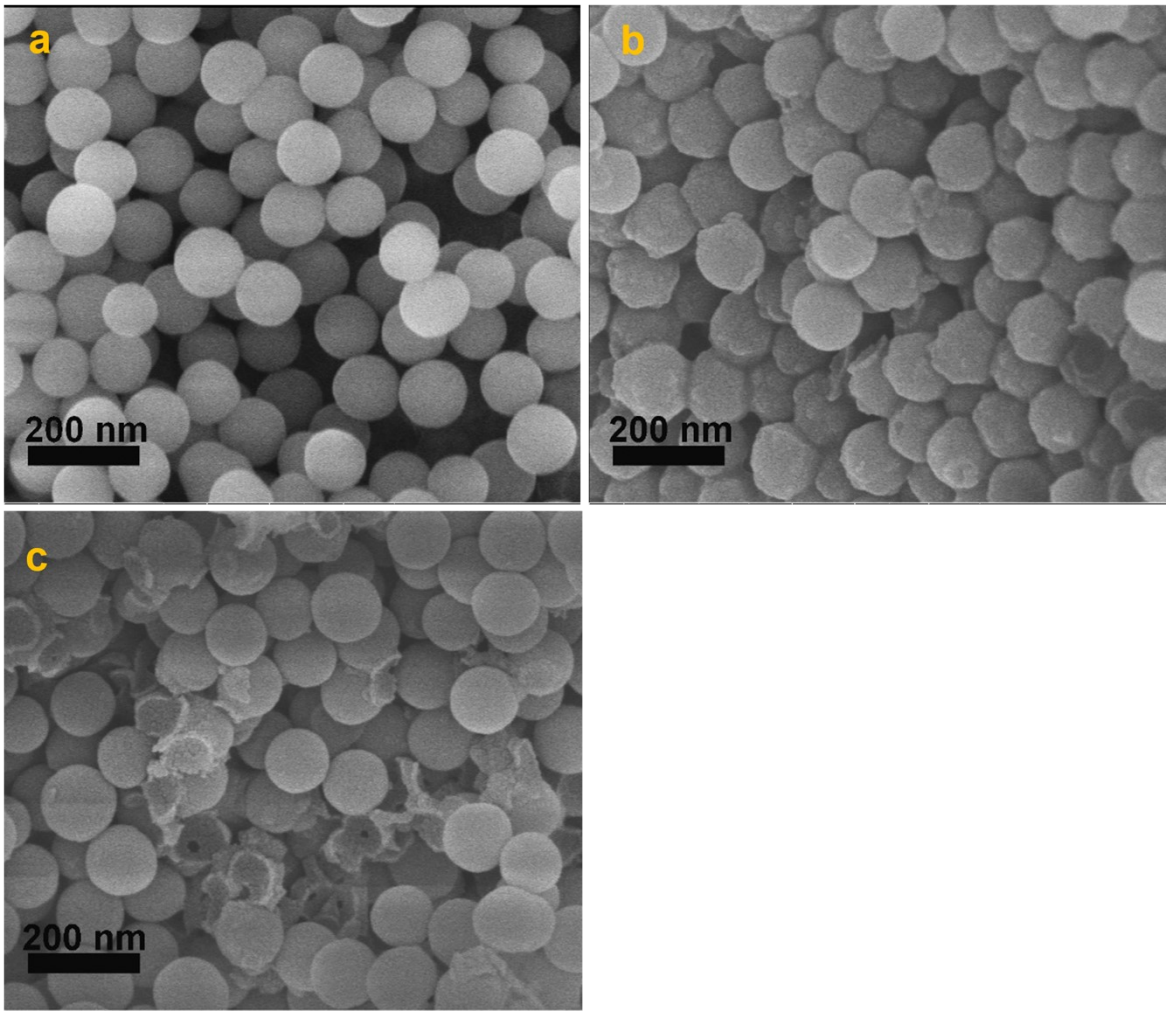

Fig. S2 FESEM images of (a) SiO_2, (b) SiO_2@PrFb and (c) *h*PrFb.

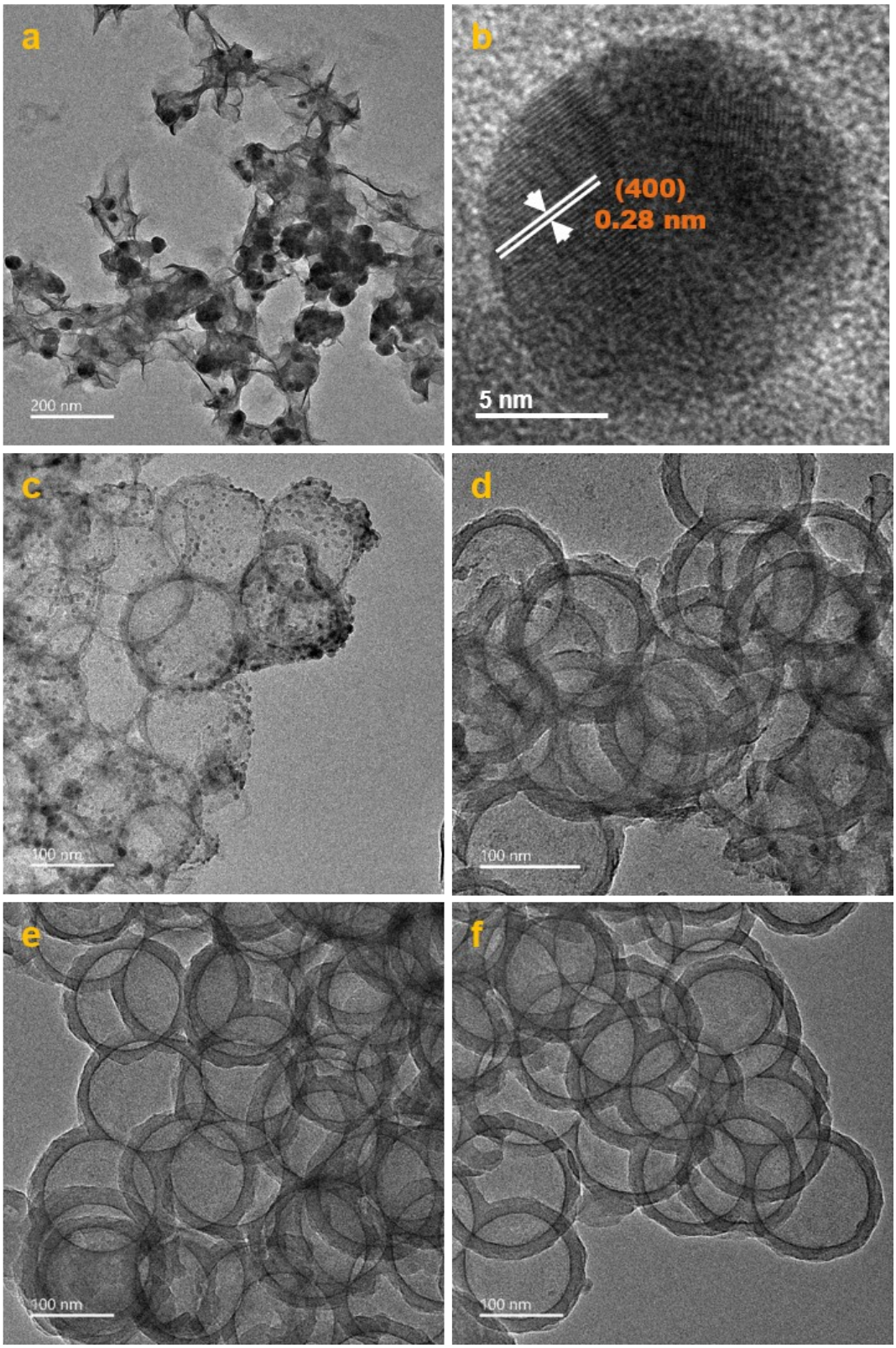

Fig. S3 TEM images of (a,b) CABB (the nanoparticles were synthesized without the *h*PrFb scaffold), (c) CABB@*h*PrFb-1, (d) CABB@*h*PrFb-4, (e) CABB@*h*PrFb-8 and (f) *h*PrFb.

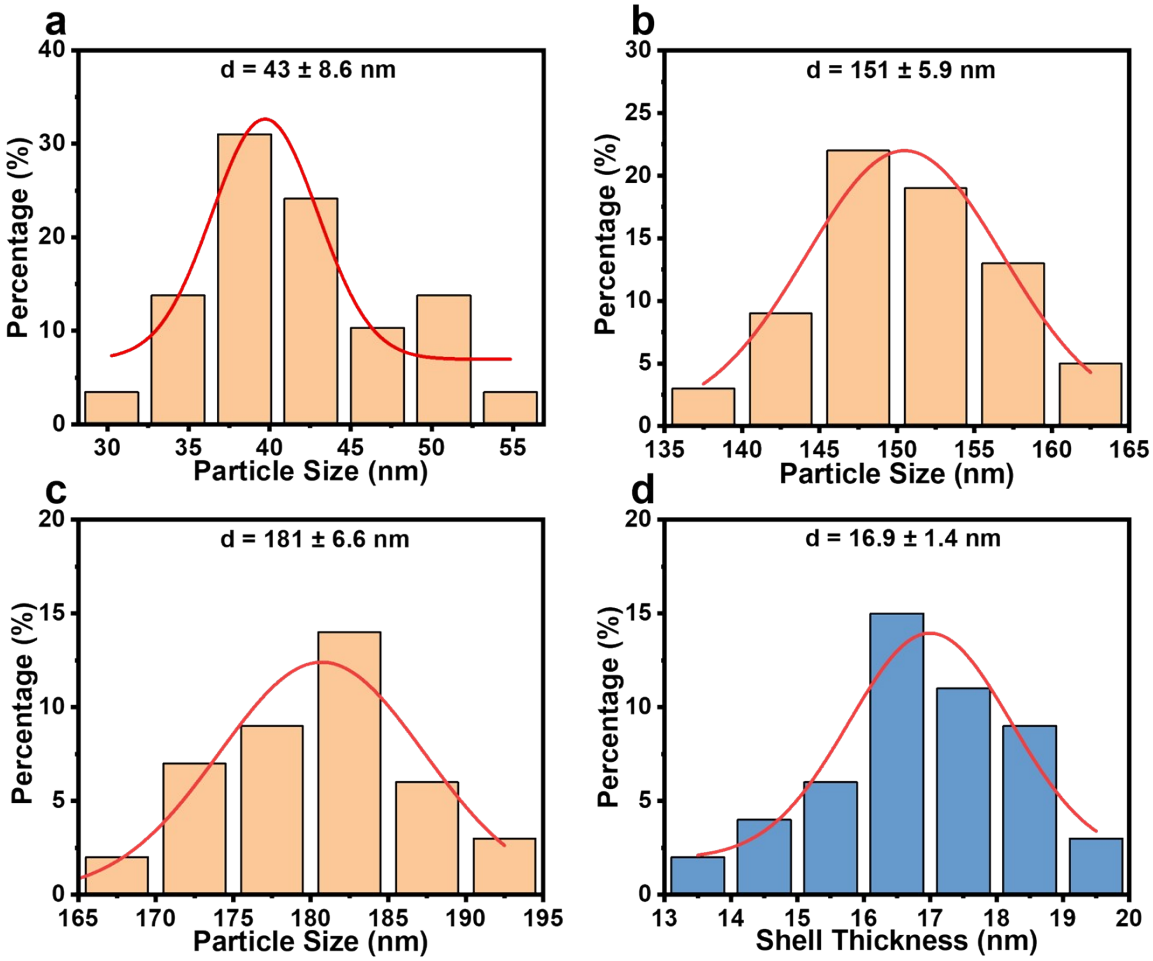

Fig. S4 Particle Size distribution of (a) CABB, (b) SiO_2 and (c) SiO_2@PrFb and shell thickness distribution of (d) *h*PrFb. The results were derived from FESEM or TEM images based on the statistical data of 50-100 nanoparticles.

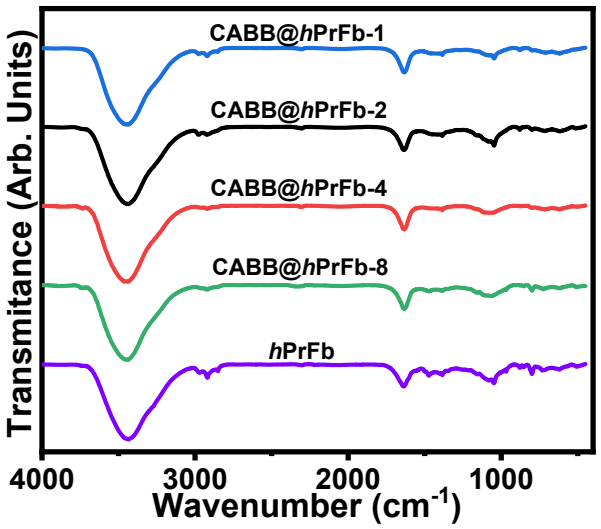

Fig. S5 FTIR spectra of CABB@*h*PrFb-1, CABB@*h*PrFb-2, CABB@*h*PrFb-4, CABB@*h*PrFb-8 and *h*PrFb.

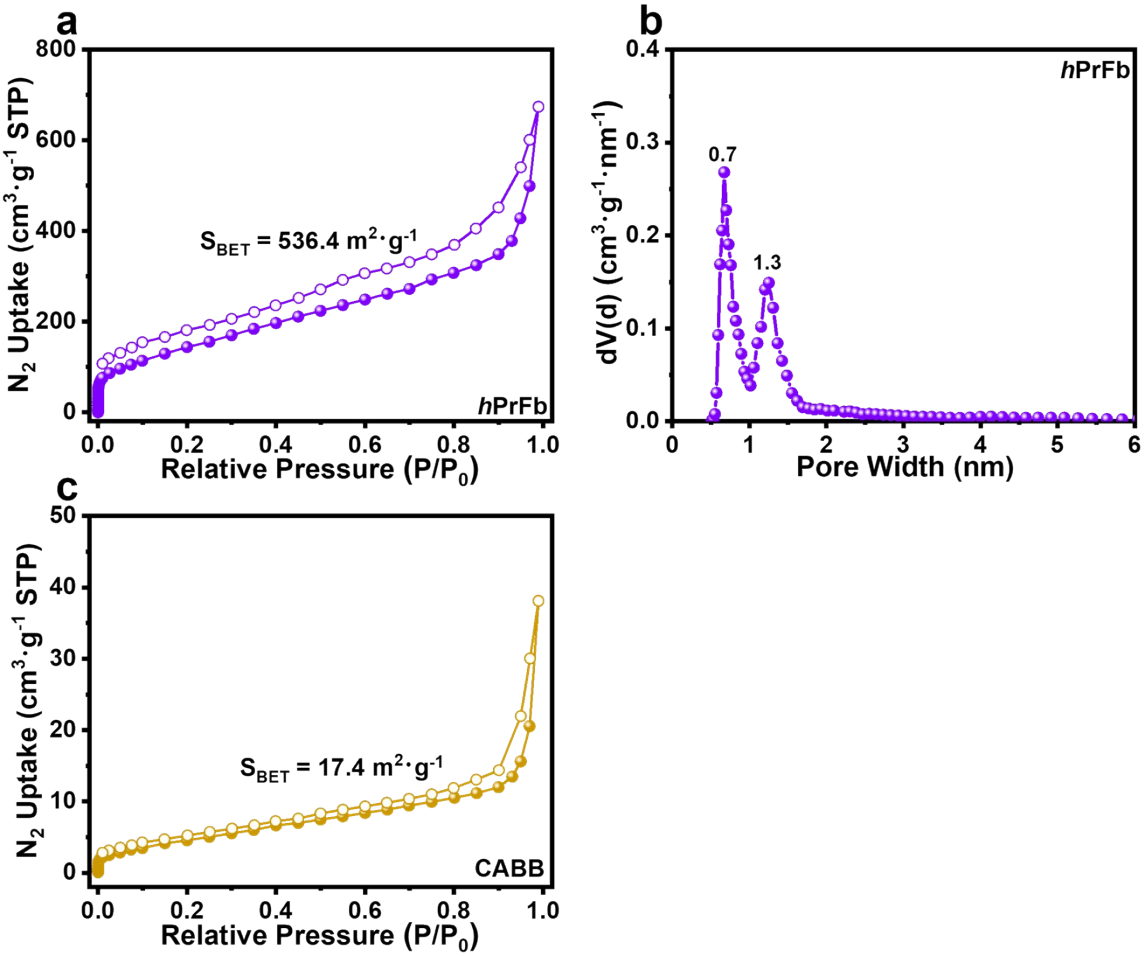

Fig. S6 BET nitrogen adsorption-desorption isotherms and pore width distribution of (a,b) *h*PrFb and (c) CABB at 77 K with respective BET surface area estimated to be 536.4 and 17.4 m^2 g^{-1}.

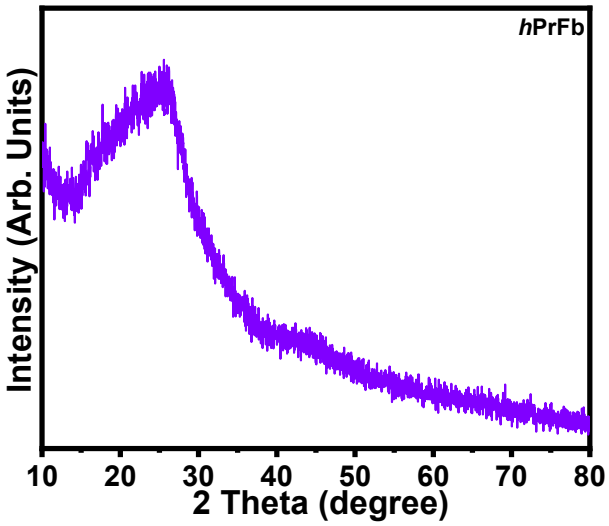

Fig. S7 XRD pattern of *h*PrFb.

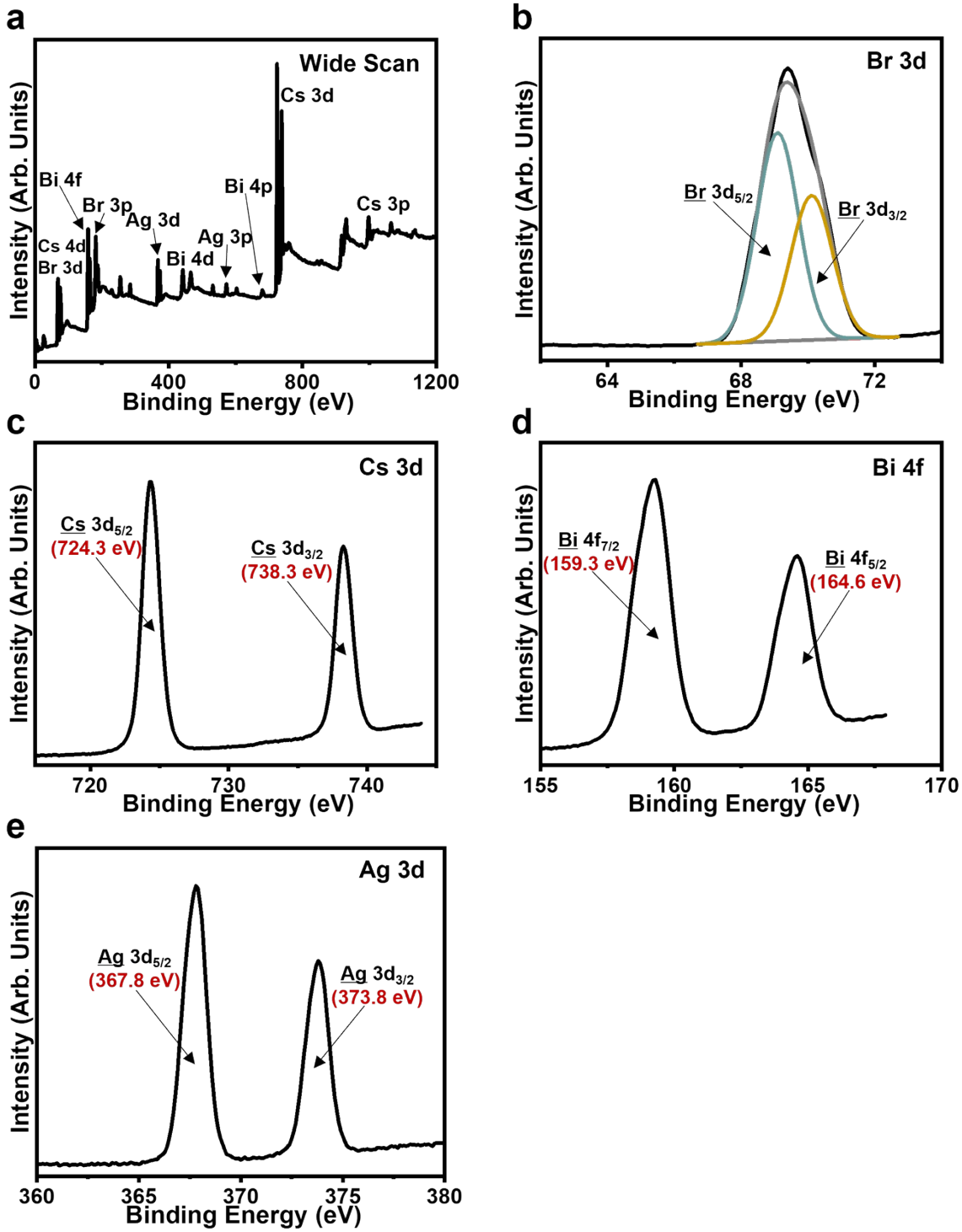

Fig. S8 XPS (a) wide scan, (b) Br 3d, (c) Cs 3d, (d) Bi 4f and (e) Ag 3d core-level spectra of CABB.

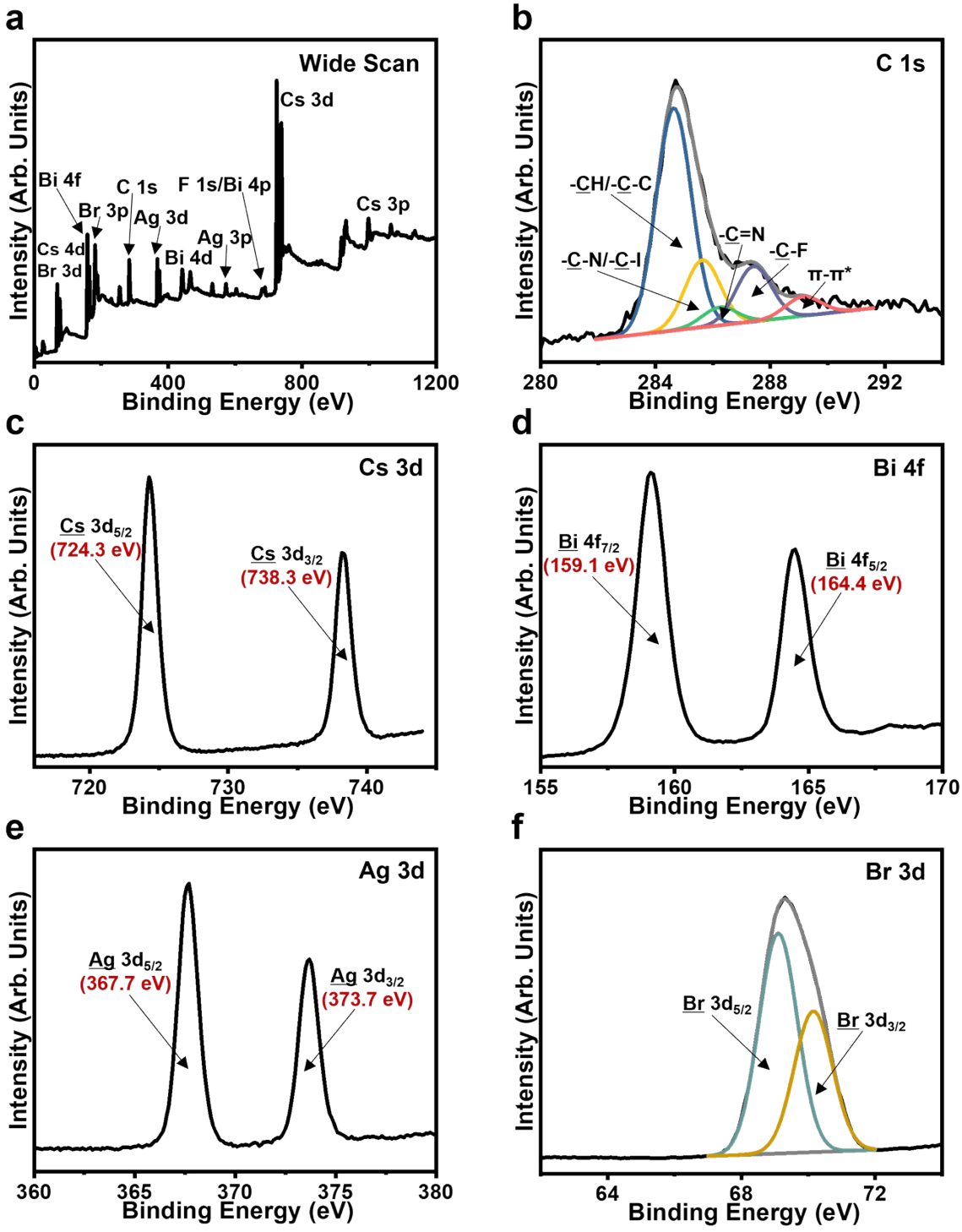

Fig. S9 XPS (a) wide scan, (b) C 1s, (c) Cs 3d, (d) Bi 4f, (e) Ag 3d and (f) Br 3d core-level spectra of CABB@*h*PrFb-1.

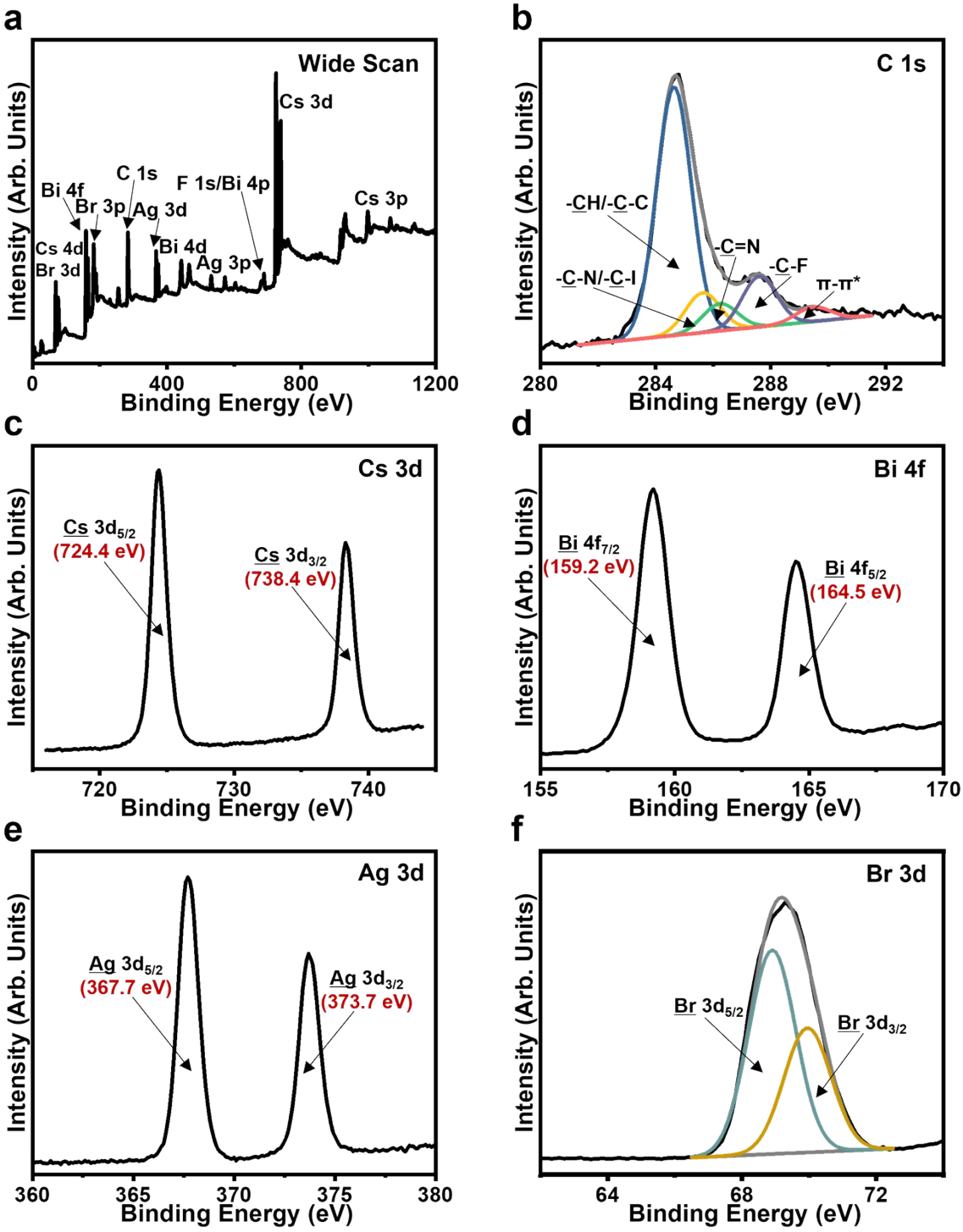

Fig. S10 XPS (a) wide scan, (b) C 1s, (c) Cs 3d, (d) Bi 4f, (e) Ag 3d and (f) Br 3d core-level spectra of CABB@*h*PrFb-2.

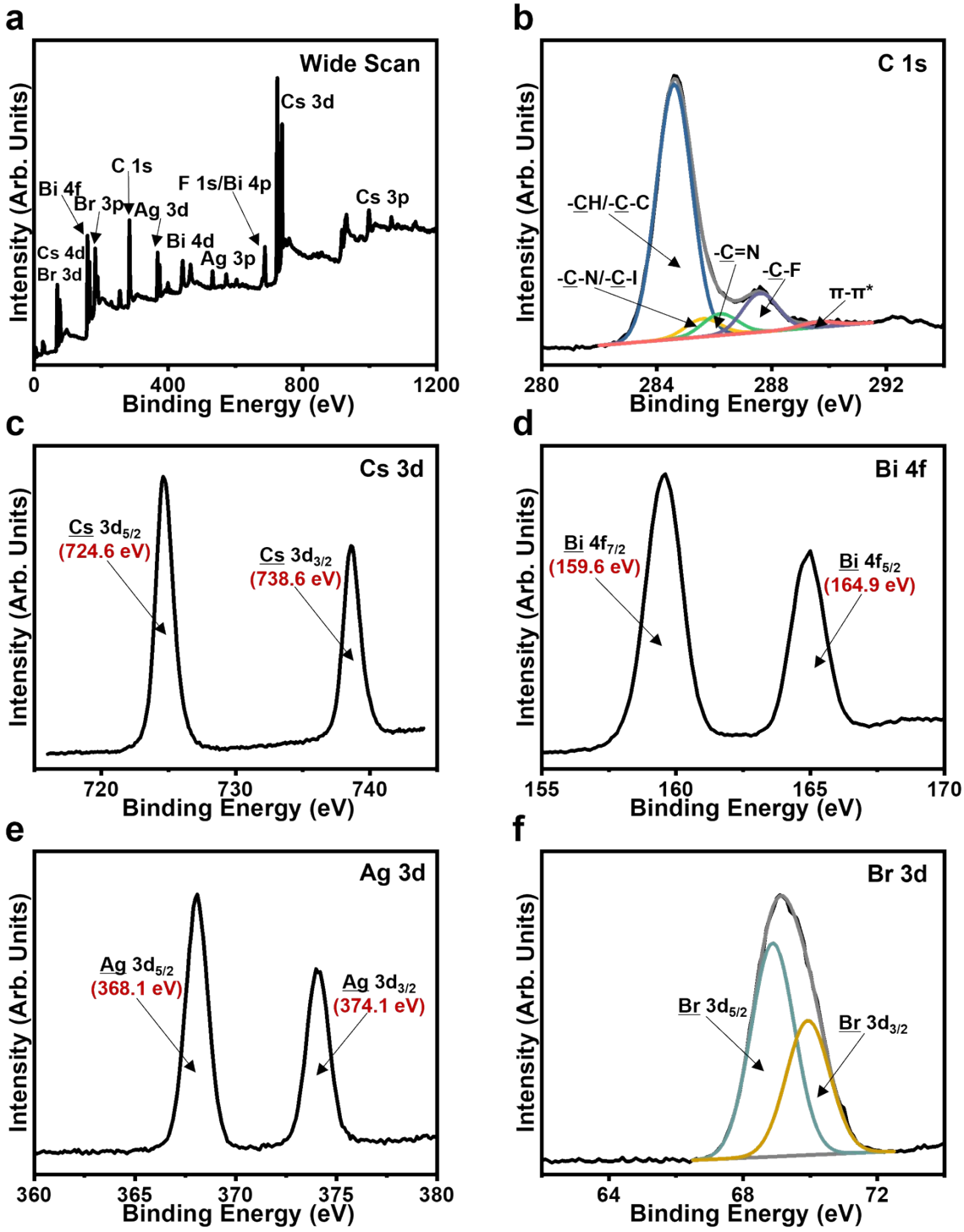

Fig. S11 XPS (a) wide scan, (b) C 1s, (c) Cs 3d, (d) Bi 4f, (e) Ag 3d and (f) Br 3d core-level spectra of CABB@*h*PrFb-4.

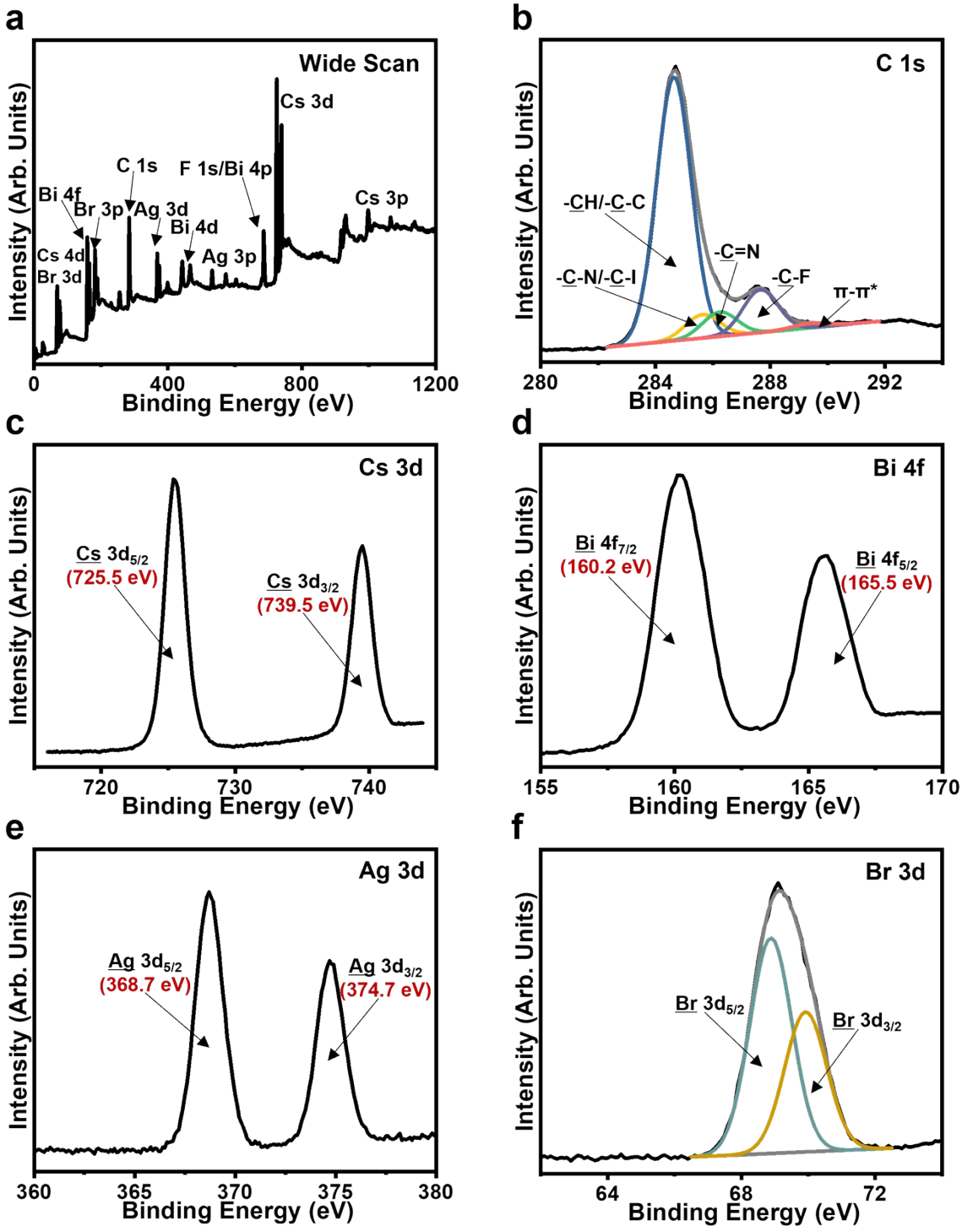

Fig. S12 XPS (a) wide scan, (b) C 1s, (c) Cs 3d, (d) Bi 4f, (e) Ag 3d and (f) Br 3d core-level spectra of CABB@*h*PrFb-8.

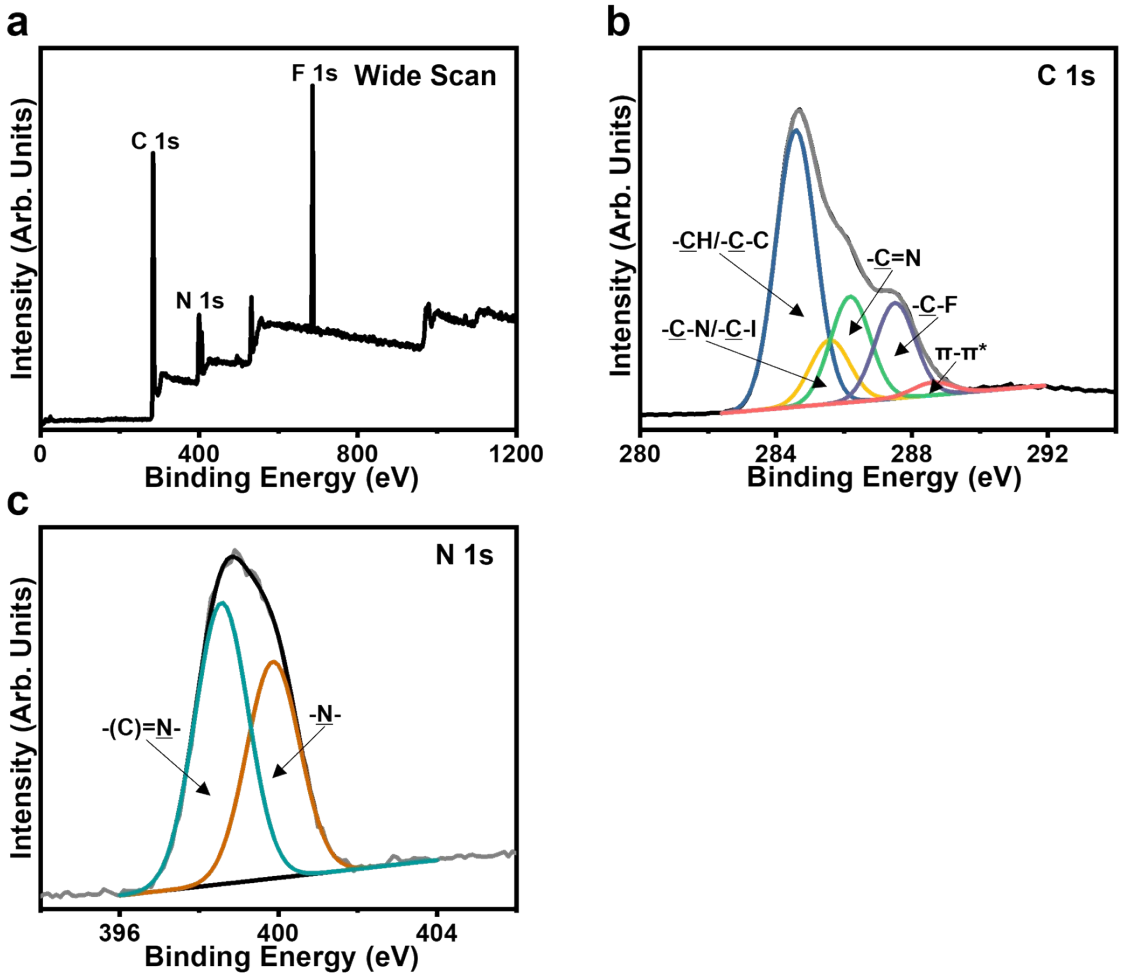

Fig. S13 XPS (a) wide scan, (b) C 1s and (c) N 1s core-level spectra of *h*PrFb.

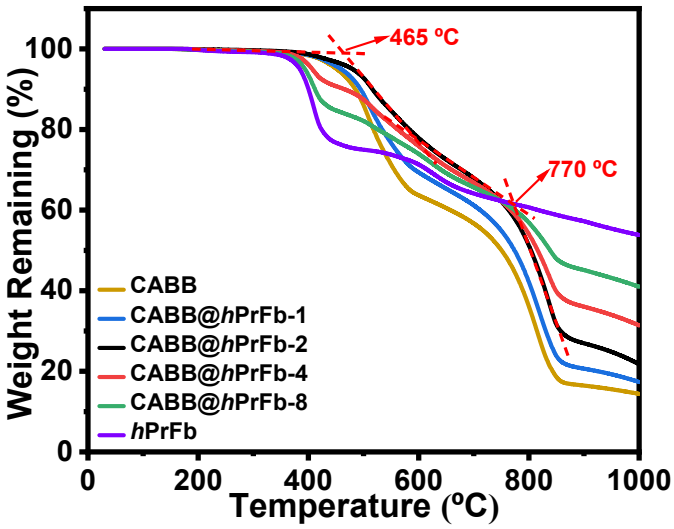

Fig. S14 TGA curves of CABB, CABB@*h*PrFb-1, CABB@*h*PrFb-2, CABB@*h*PrFb-4, CABB@*h*PrFb-8 and *h*PrFb.

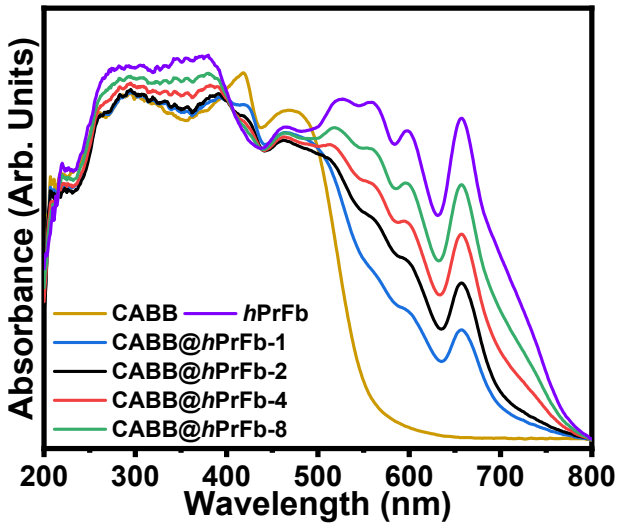

Fig. S15 UV-vis DR spectra of CABB, CABB@*h*PrFb-1, CABB@*h*PrFb-2, CABB@*h*PrFb-4, CABB@*h*PrFb-8 and *h*PrFb.

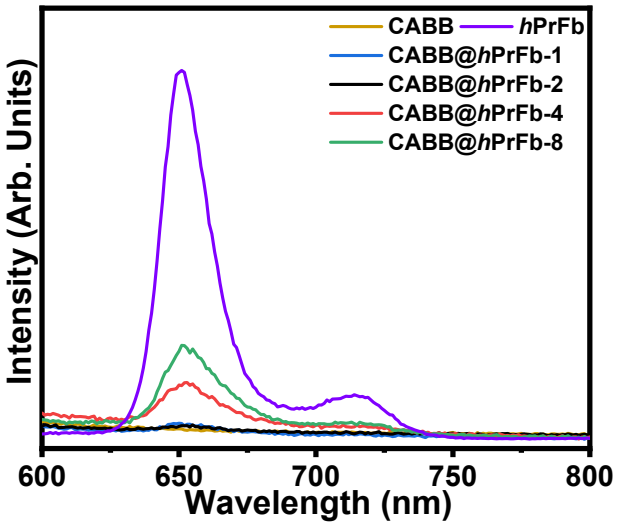

Fig. S16 PL spectra of CABB, CABB@*h*PrFb-1, CABB@*h*PrFb-2, CABB@*h*PrFb-4, CABB@*h*PrFb-8 and *h*PrFb.

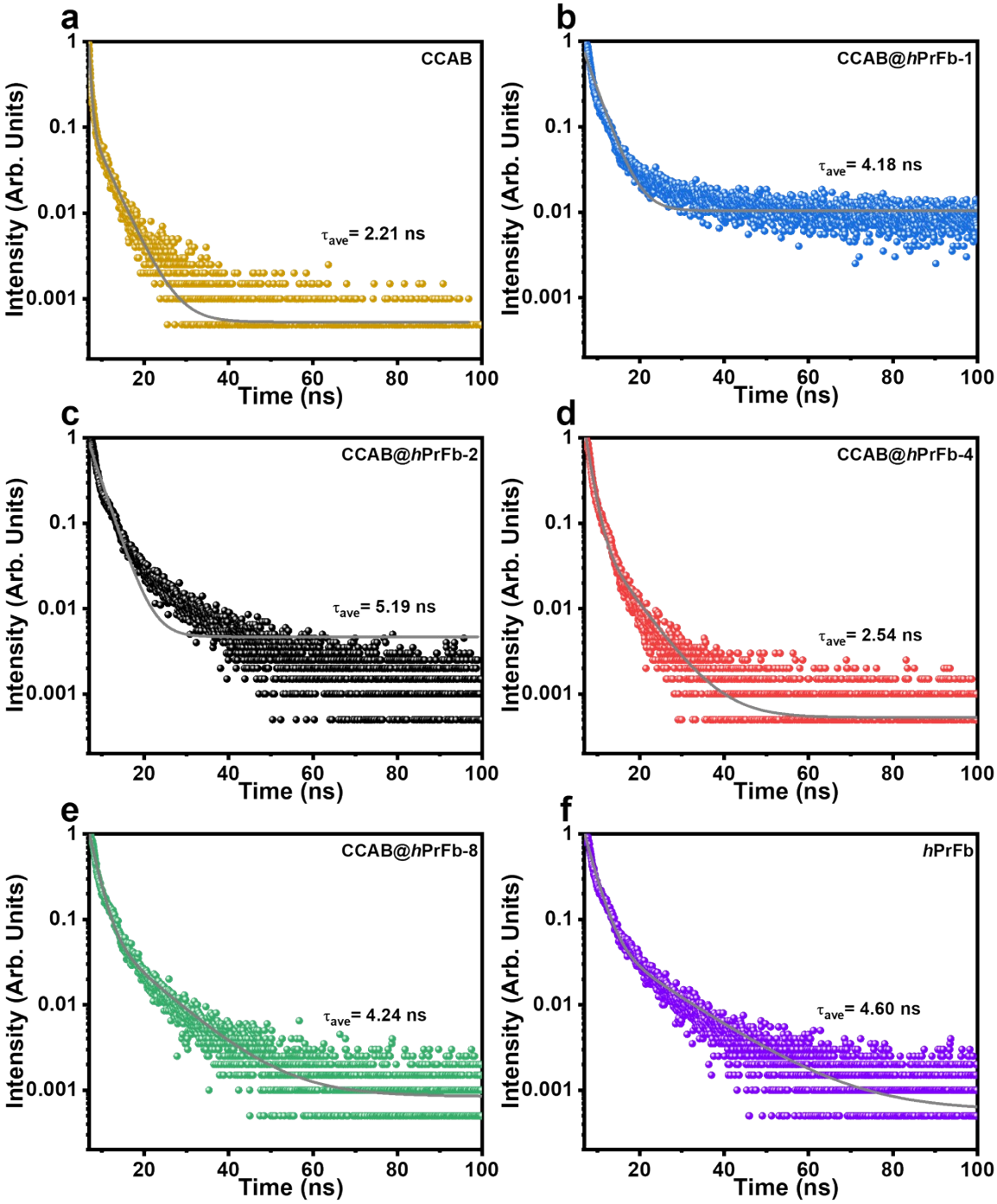

Fig. S17 TRPL spectra for (a) CABB, (b) CABB@*h*PrFb-1, (c) CABB@*h*PrFb-2, (d) CABB@*h*PrFb-4, (e) CABB@*h*PrFb-8 and (f) *h*PrFb. CABB was excited with a λ_{exc} = 420 nm laser and the other samples were excited with a λ_{exc} = 500 nm laser.

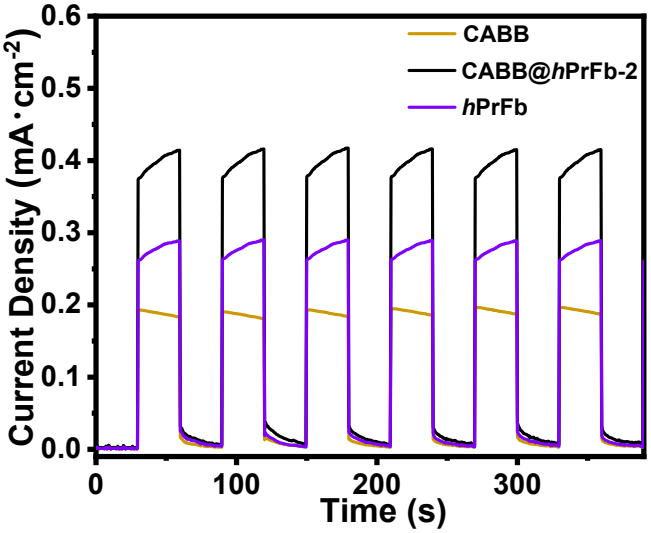

Fig. S18 Transient photocurrent (TPC) responses of CABB, CABB@*h*PrFb-2 and *h*PrFb.

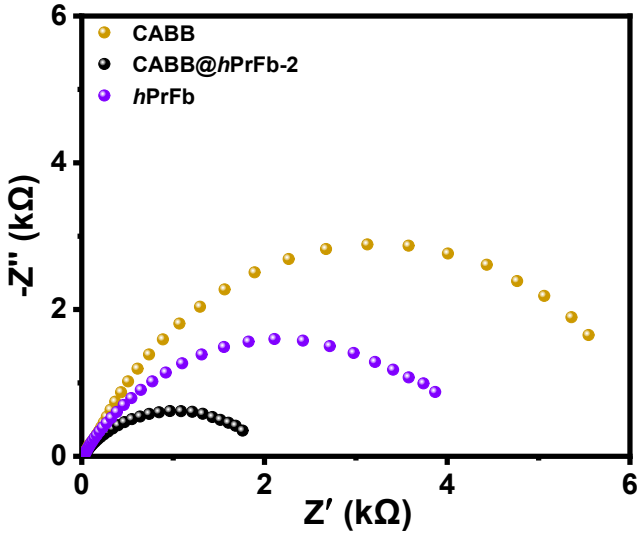

Fig. S19 EIS Nyquist plots of CABB, CABB@*h*PrFb-2 and *h*PrFb.

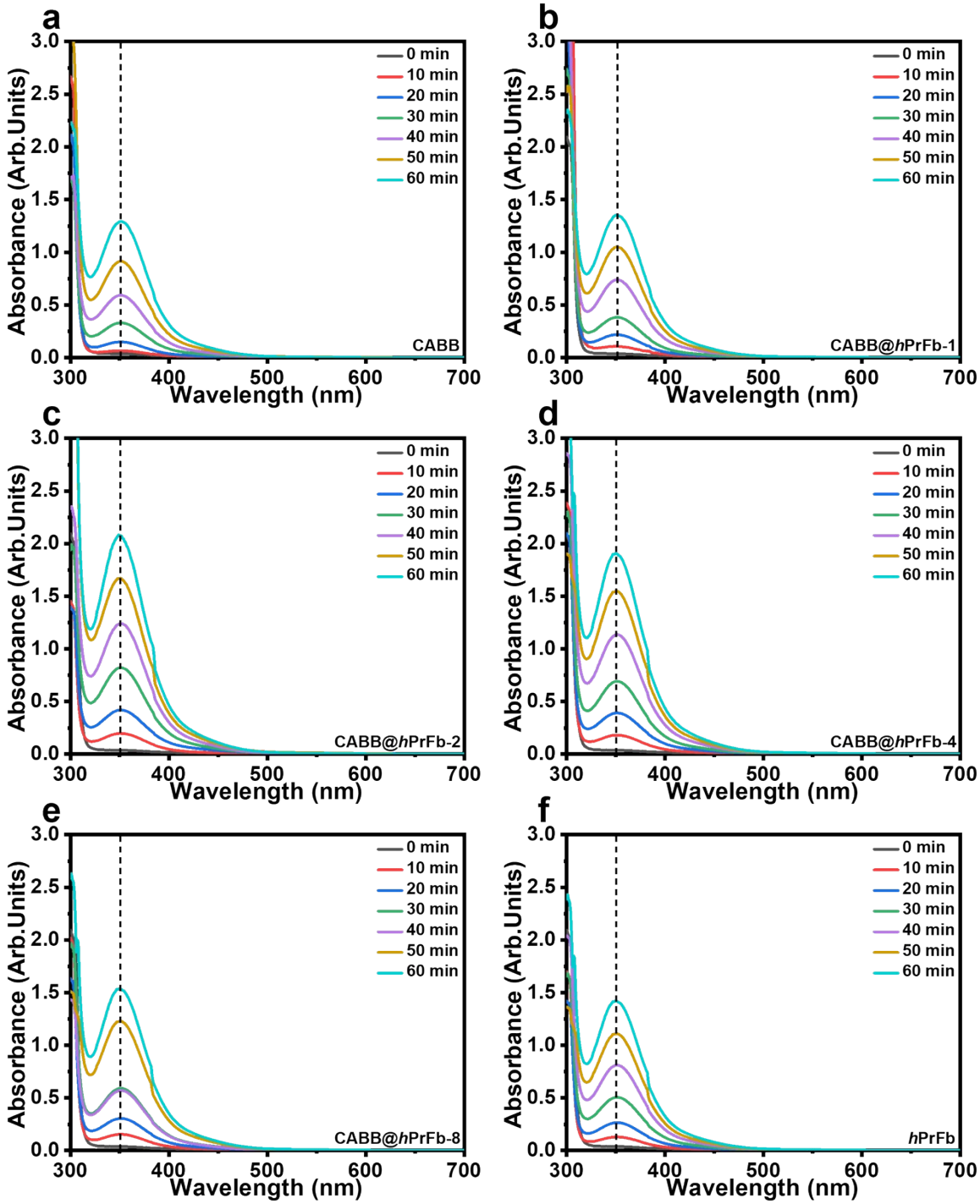

Fig. S20 UV-vis absorbance spectra of photocatalytic H_2O_2 production containing (a) CABB, (b) CABB@*h*PrFb-1, (c) CABB@*h*PrFb-2, (d) CABB@*h*PrFb-4, (e) CABB@*h*PrFb-8 and (f) *h*PrFb.

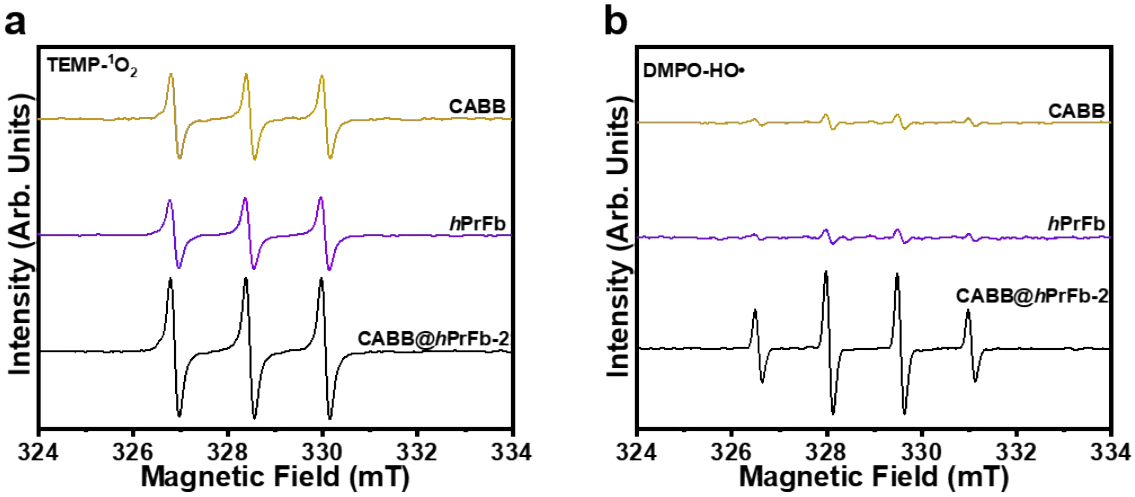

Fig. S21 (a,b) EPR spectra of CABB, CABB@*h*PrFb-2 and *h*PrFb with TEMP and DMPO under dark conditions or white LED light irradiation.

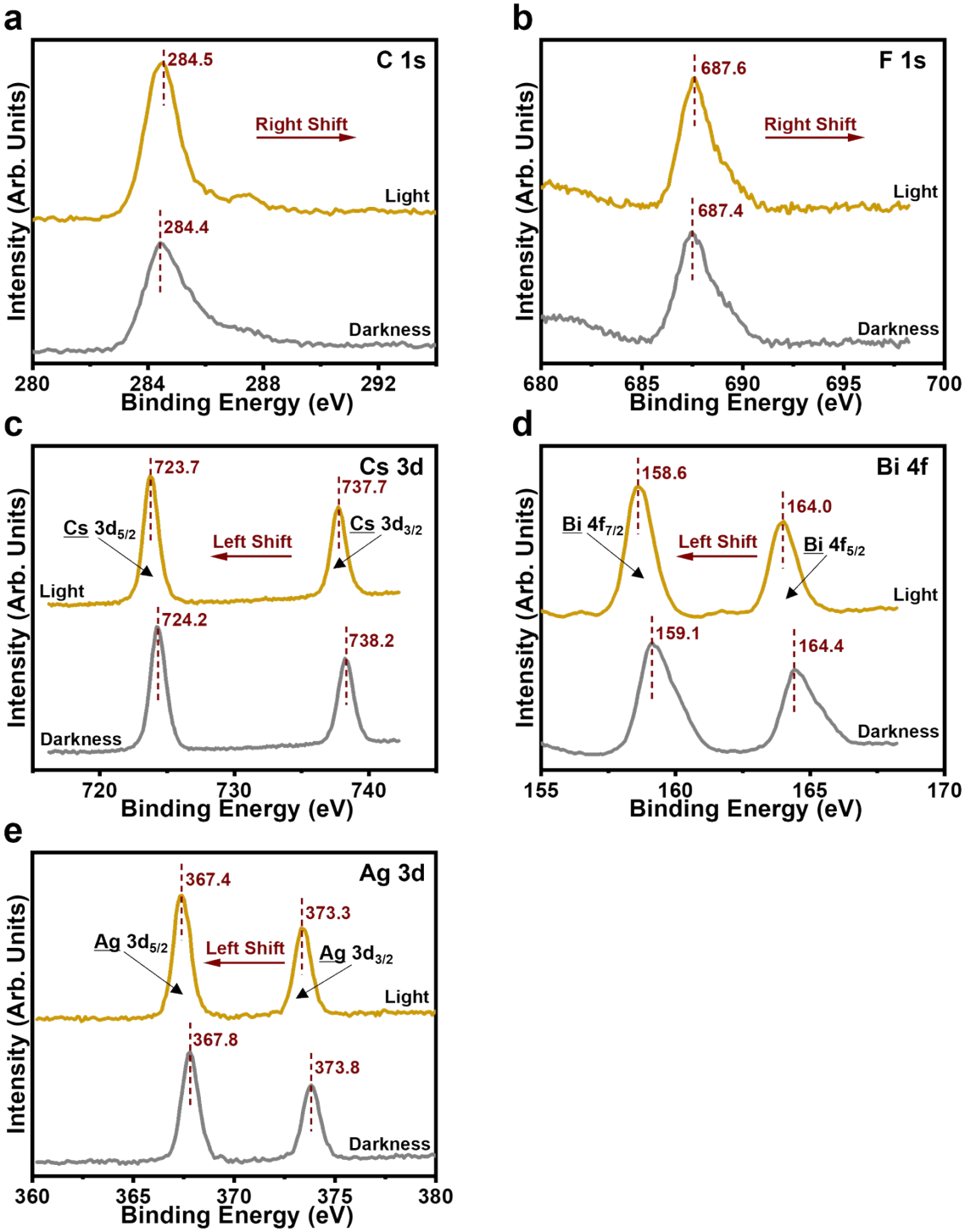

Fig. S22 In-situ XPS spectra of (a) C 1s, (b) F 1s, (c) Cs 3d, (d) Bi 4f and (e)) Ag 3d for CABB@*h*PrFb-2 under dark conditions or light irradiation.

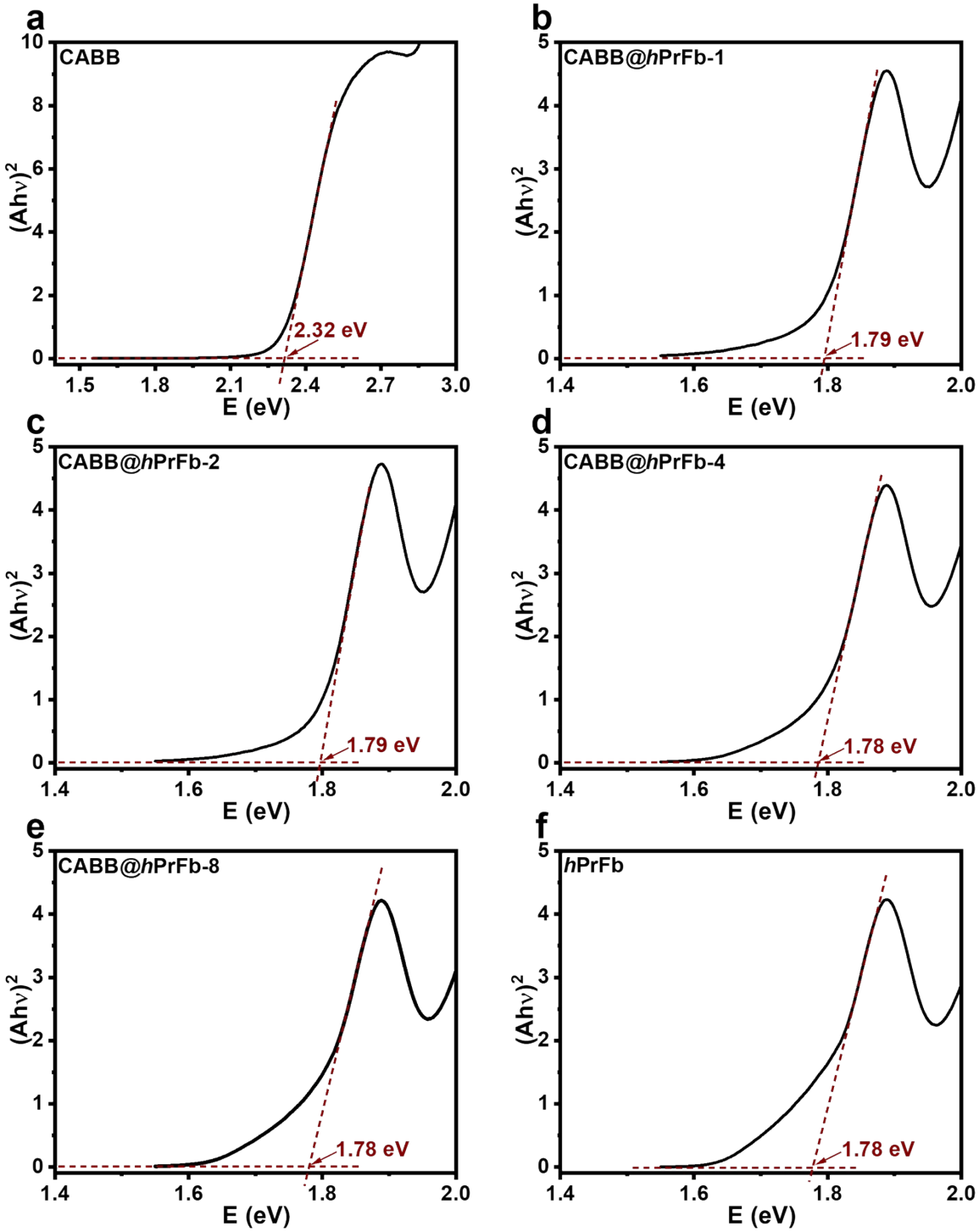

Fig. S23 Kubelka-Munk plots for the calculated bandgap energies of (a) CABB, (b) CABB@*h*PrFb-1, (c) CABB@*h*PrFb-2, (d) CABB@*h*PrFb-4, (e) CABB@*h*PrFb-8 and (f) *h*PrFb.

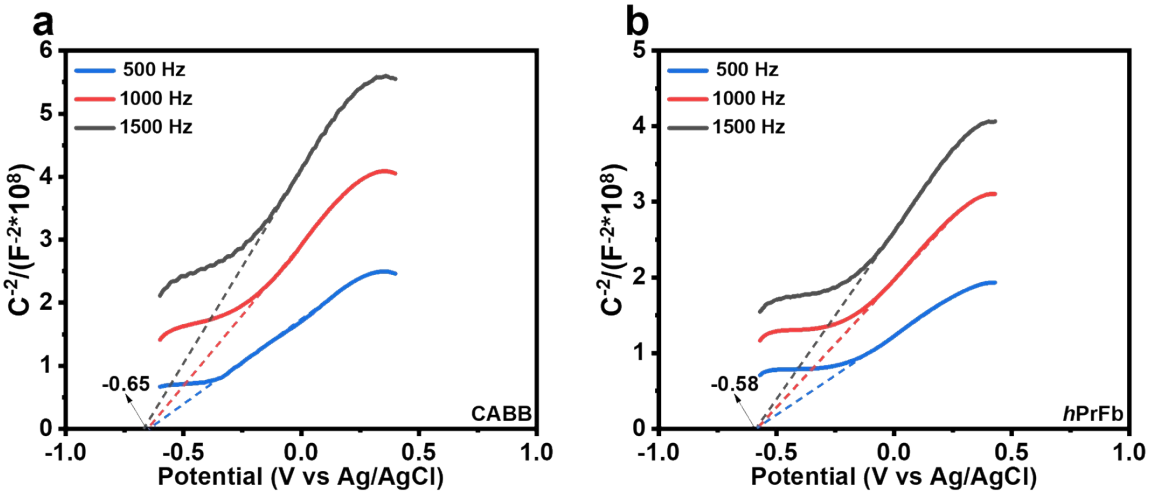

Fig. S24 Mott-Schottky plots of (a) CABB and (b) *h*PrFb.

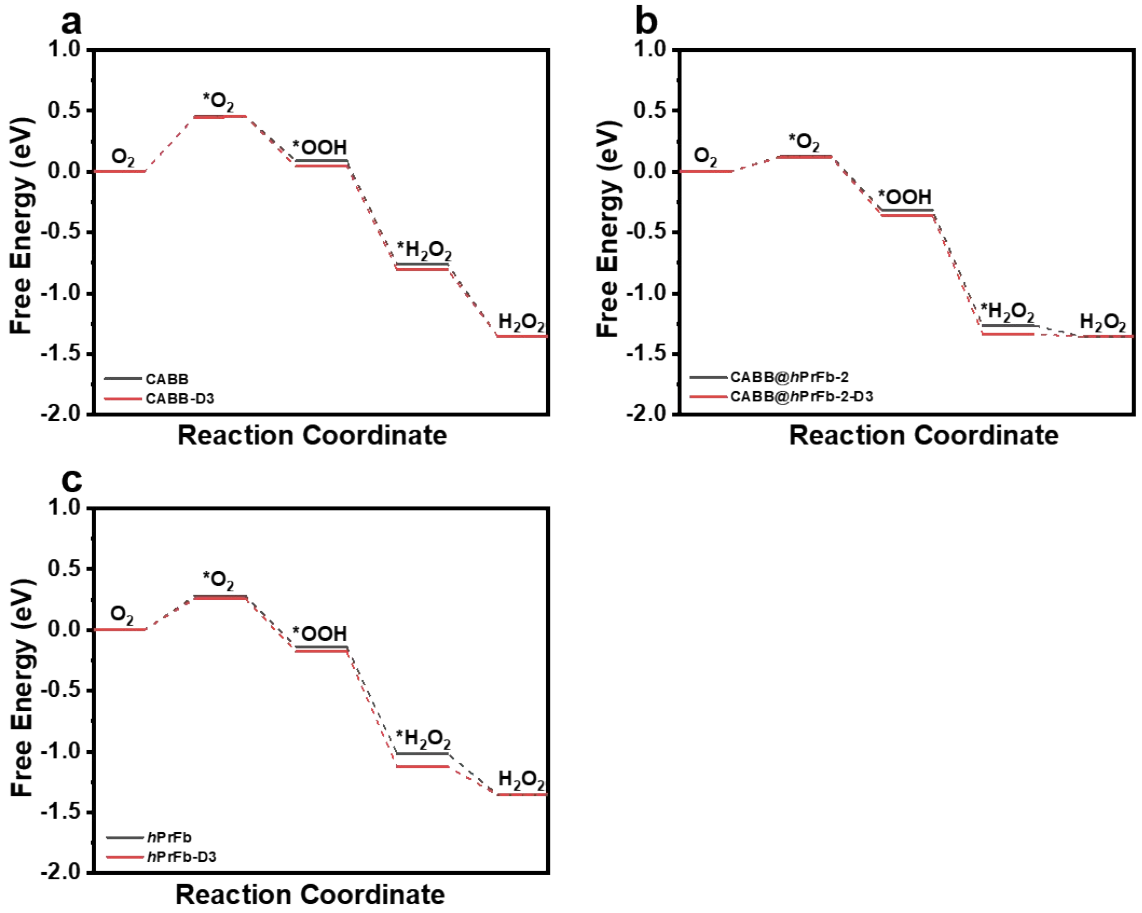

Fig. S25 The vdW correction for (a) CABB, (b) CABB@*h*PrFb-2 and (c) *h*PrFb. To accurately describe the non-covalent interaction (e.g., dispersion forces) with the system, the van der Waals correction was incorporated using the Grimme's DFT-D3 method (DFT-D3) in all calculations.[18,19]

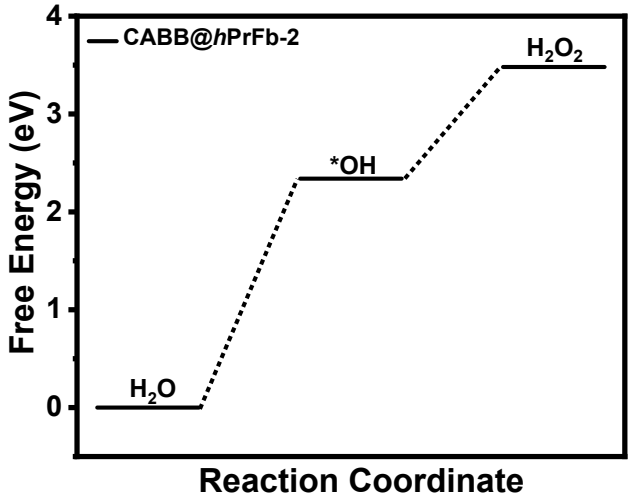

Fig. S26 Gibbs free energy diagrams of WOR steps on CABB@*h*PrFb-2.

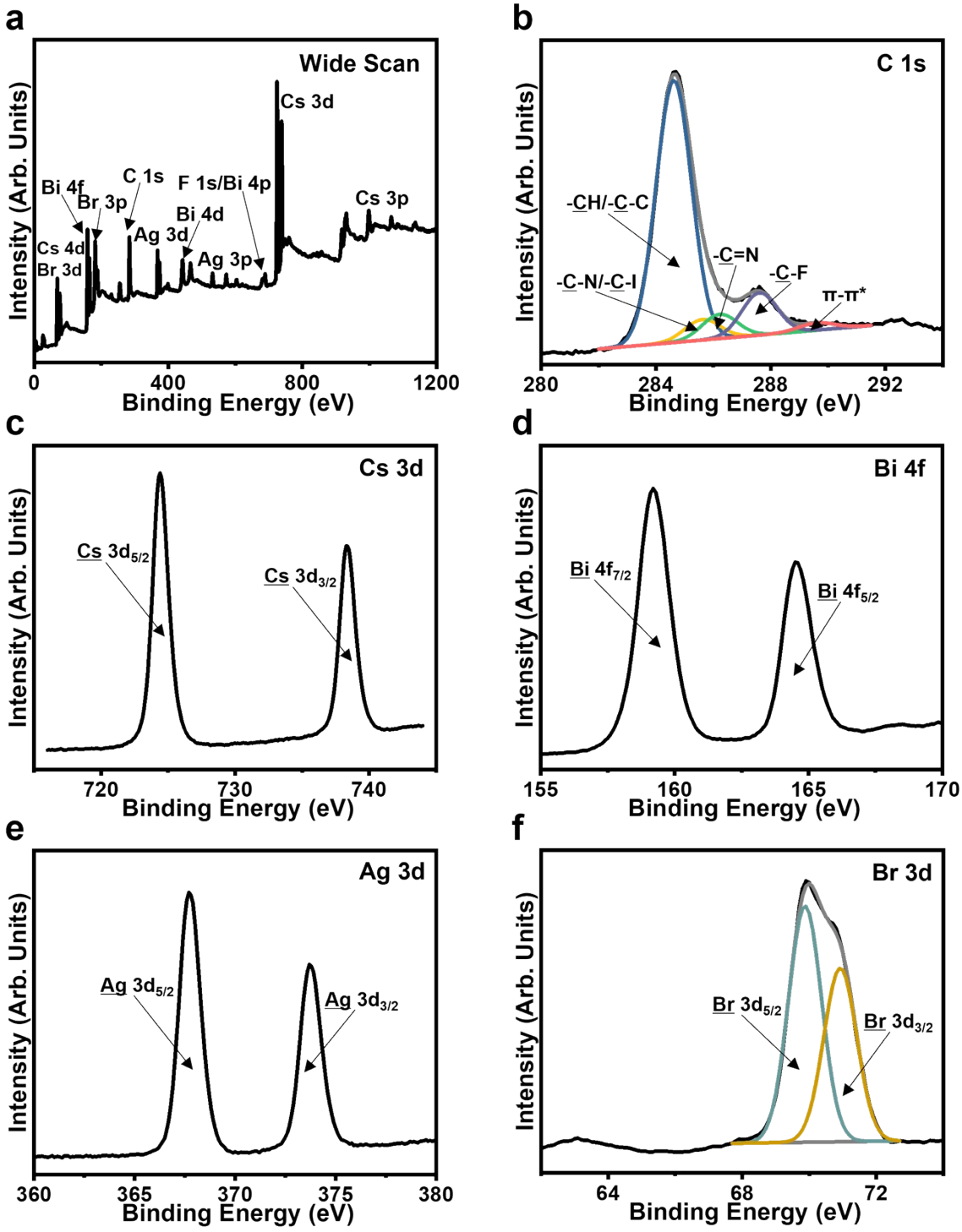

Fig. S27 XPS (a) wide scan, (b) C 1s, (c) Cs 3d, (d) Bi 4f, (e) Ag 3d and (f) Br 3d core-level spectra of CABB@*h*PrFb-2 after eight reaction cycles.

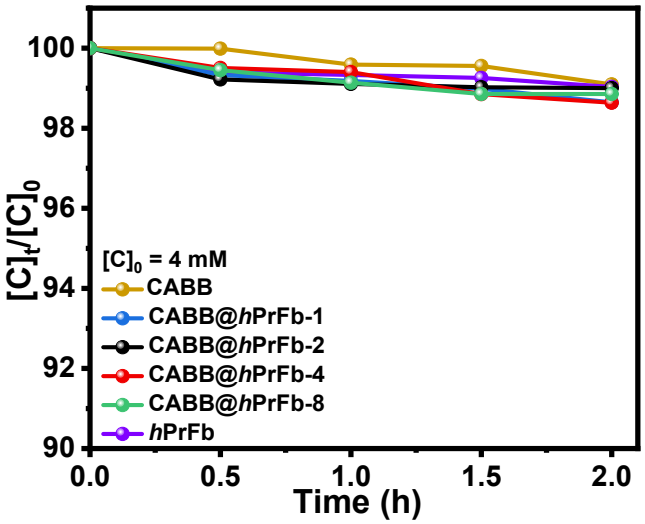

Fig. S28 The decomposition rate diagrams of H_2O_2 for CABB, CABB@*h*PrFb-1, CABB@*h*PrFb-2, CABB@*h*PrFb-4, CABB@*h*PrFb-8 and *h*PrFb within 2 h.

Table S1. XPS Results of CABB@*h*PrFb in This Study

Sample	C(%)	N(%)	O(%)	F(%)	Cs(%)	Bi(%)	Ag(%)	Br(%)	Ag/C
CABB	-	-	-	-	25.03	8.61	7.77	58.58	-
CABB@*h*PrFb-1	28.42	8.43	7.63	17.22	10.09	3.51	3.01	21.69	0.106
CABB@*h*PrFb-2	34.41	10.04	11.50	20.28	5.84	2.30	1.98	13.65	0.058
CABB@*h*PrFb-4	38.54	12.07	11.74	24.25	3.37	1.16	1.04	7.83	0.027
CABB@*h*PrFb-8	41.72	13.10	12.03	25.92	1.81	0.63	0.59	4.20	0.014
*h*PrFb	44.46	13.93	13.75	27.86	-	-	-	-	-
CABB@*h*PrFb-2 (After eight reaction cycles)	34.81	10.27	11.79	20.33	5.77	2.15	1.94	12.94	0.056

Table S2. Comparison of Binding Energy in the Composite Nanoparticles

Sample	Cs 3d	ΔBE	Bi 4f	ΔBE	Ag 3d	ΔBE	C 1s	ΔBE
CABB	724.3, 738.3	0	159.3, 164.6	0	367.8, 373.8	0	-	-
*h*PrFb	-	-	-	-	-	-	284.2	0
CABB@*h*PrFb-1	724.3, 738.3	0	159.1, 164.4	-0.2	367.7, 373.7	-0.1	284.1	-0.1
CABB@*h*PrFb-2	724.4, 738.4	+0.1	159.2, 164.5	-0.1	367.7, 373.7	-0.1	284.2	0
CABB@*h*PrFb-4	724.6, 738.6	+0.3	159.6, 164.9	+0.3	368.1, 374.1	+0.3	284.2	0
CABB@*h*PrFb-8	725.5, 739.5	+1.2	160.2, 165.5	+0.9	368.7, 374.7	+0.9	284.2	0

Table S3. Comparison of Perovskite-Based Photocatalysts Mediated Photocatalytic Generation of H_2O_2

#	Photocatalyst	Catalyst Dosage (mg mL^{-1})	Light Source	Oxidant	Additive	H_2O_2 Production (μmol g^{-1} h^{-1})	Circular Cycles	Ref.
1	CABB@*h*PrFb-2	0.125	300 W Xe Lamp	O_2	-	3500	8	This Work
2	Ru@Cu-HHTP-3	0.2	300 W Xe Lamp	O_2	10 vol% Ethanol	571	4	[17]
3	0.5CQD-CTF	0.25	300 W Xe Lamp	O_2	-	1036	5	[20]
4	0.50CuTi(AR)P	0.75	300 W Xe Lamp	O_2	10 vol% Methanol	1175	5	[21]
5	Py/HTCC	0.2	300 W Xe Lamp	O_2	-	1438	10	[22]
6	$Mn_{0.2}Cd_{0.8}S$	0.2	300 W Xe Lamp	Air	-	1522	4	[23]
7	Co_1@(c-BP/a-RP)	0.4	300 W Xe Lamp	O_2	-	2497	4	[24]
8	CNZIS	0.5	300 W Xe Lamp	O_2	10 vol% Propanol	1592	4	[25]
9	PBNCZ-COO-	0.6	300 W Xe Lamp	Air	-	1719	Not Provided	[26]
10	NiPC/TS-0.35	0.2	300 W Xe Lamp	O_2	10 vol% Propanol	1744	5	[27]
11	PCN	2	300 W Xe Lamp	Air	-	2063	10	[28]
12	In_2S_3/CdS	0.4	300 W Xe Lamp	O_2	-	2090	4	[29]
13	40% K^+/I^-—CN/CdSe-D	0.2	300 W Xe Lamp	O_2	10 vol% Ethanol	2240	4	[30]
14	Cd-SV/ZIS	0.25	300 W Xe Lamp	O_2	-	2365	5	[31]
15	MTPLi-K	0.143	300 W Xe Lamp	Air	10 vol% Propanol	2807	6	[32]
16	BTZ-3	0.25	300 W Xe Lamp	O_2	-	3267	4	[33]

Table S4. Control Experiments for Photocatalytic H_2O_2 Production Using CABB@*h*PrFb as the Catalysts[a]

#	Catalyst	Atmosphere	Light Source	Catalyst Amount	Additive[b]	Rection Time (h)	H_2O_2 Production ($\mu mol\ g^{-1}\ h^{-1}$)[c]
1	CABB@*h*PrFb-2	O_2	300 W Xe lamp	5 mg	No	0.5	2749
2	CABB@*h*PrFb-2	O_2	300 W Xe lamp	5 mg	No	1	3500
3	CABB	O_2	300 W Xe lamp	5 mg	No	1	2153
4	CABB@*h*PrFb-1	O_2	300 W Xe lamp	5 mg	No	1	2253
5	CABB@*h*PrFb-4	O_2	300 W Xe lamp	5 mg	No	1	3215
6	CABB@*h*PrFb-8	O_2	300 W Xe lamp	5 mg	No	1	2579
7	*h*PrFb	O_2	300 W Xe lamp	5 mg	No	1	2379
8	-	O_2	300 W Xe lamp	-	No	1	0
9	CABB@*h*PrFb-2	O_2	-	5 mg	No	1	6
10	CABB@*h*PrFb-2	Air	300 W Xe lamp	5 mg	No	1	2605
11	CABB@*h*PrFb-2	Ar	300 W Xe lamp	5 mg	No	1	82
12	CABB@*h*PrFb-2	Ar	300 W Xe lamp	5 mg	0.01 mM $AgNO_3$	1	60
13	CABB@*h*PrFb-2	O_2	300 W Xe lamp	5 mg	0.01 mM $AgNO_3$	1	87
14	CABB@*h*PrFb-2	O_2	300 W Xe lamp	5 mg	10 vol% BA	1	10200
15	CABB@*h*PrFb-2	O_2	300 W Xe lamp	5 mg	0.01 mM BQ	1	76
16	CABB@*h*PrFb-2	O_2	300 W Xe lamp	5 mg	0.1 mM NaN_3	1	313
17	CABB@*h*PrFb-2	O_2	300 W Xe lamp	5 mg	1 mM TBA	1	2817

Notes: [a]Conditions: photocatalyst (5 mg), ultrapure water (40 mL). [b]Abbreviation: BA, benzyl alcohol; BQ, benzoquinone; TBA, *tert*-butyl alcohol. [c]Conversion determined by UV-vis spectroscopy.

References

[1] G. Kresse, J. Furthmüller, *Comput. Mater. Sci.*, 1996, **6**, 15-50.

[2] G. Kresse, J. Furthmüller, *Phys. Rev. B*, 1996, **54**, 11169-11186.

[3] J. P. Perdew, K. Burke, M. Ernzerhof, *Phys. Rev. Lett.*, 1996, **77**, 3865-3868.

[4] G. Kresse, D. Joubert, *Phys. Rev. B*, 1999, **59**, 1758-1775.

[5] P. E. Blöchl, *Phys. Rev. B*, 1994, **50**, 17953-17979.

[6] H. J. Monkhorst, J. D. Pack, *Phys. Rev. B*, 1976, **13**, 5188.

[7] D. Hobbs, G. Kresse, J. Hafner, *Phys. Rev. B*, 2000, **62**, 11556.

[8] A. A. Mostofi, J. R. Yates, G. Pizzi, Y. S. Lee, I. Souza, D. Vanderbilt, N. Marzari, *Comput. Phys. Commun.*, 2014, **185**, 2309.

[9] Q. Wu, S. Zhang, H. F. Song, M. Troyer, A. A Soluyanov, *Comput. Phys. Commun.*, 2018, **224**, 405-416.

[10] Y. W. Duan, X. J. Zhang, W. L. Guo, M. Jian, T. Cai, X. Li, *J. Mater. Chem. A*, 2023, **11**, 4639-4650.

[11] X. Li, X. J. Zhang, W. L. Guo, Y. Huang, T. Cai, *Chem. Eng. J.*, 2023, **465**, 142861.

[12] Y. Huang, Q. Xiang, X. Li, T. Cai, *Macromolecules*, 2024, **57**, 5081-5091.

[13] Q. Xiang, Y. Huang, S. H. Jiang, S. X. Cheng, X. Li, T. Cai, *Adv. Funct. Mater.*, 2024, **34**, 2400512.

[14] X. Li, Y. Huang, M. Jian, X. J. Zhang, T. Cai, *Macromolecules*, 2023, **56**, 6152-6161.

[15] K. Cho, C. W. Kang, S. H. Ryu, J. Y. Jang, S. U. Son, *J. Mater. Chem. A*, 2022, **10**, 6950-6964.

[16] S. Gao, G. He, B. Wang, Q. Li, X. Chen, D. Mei, J. Yu, *J. Am. Chem. Soc.*, 2025, **147**, 35975-35984.

[17] C. Feng, J. Alharbi, M. Hu, S. Zuo, J. Luo, H. S. Al Qahtani, M. Rueping, K. W. Huang, H. Zhang, *Adv. Mater.*, 2025, **37**, 2406748.

[18] S. Grimme, *J. Comput. Chem.*, 2006, **27**, 1787.

[19] S. Grimme, J. Antony, S. Ehrlich, H. Krieg, *J. Chem. Phys.*, 2010, **132**, 15410.

[20] Y. Yang, Q. Guo, Q. Li, L. Guo, H. Chu, L. Liao, X. Wang, Z. Li, W. Zhou, *Adv. Funct. Mater.*, 2024, **34**, 2400612.

[21] F. Sun, Q. Xu, X. Wang, C. Luo, M. Zhao, Q. Ma, H. Yu, W. Yu, X. Dong, *Adv. Funct. Mater.*, 2025, **35**, e05795.

[22] Y. Wu, S. Yan, L. Wang, L. Chen, Y. Li, K. Shen, *Appl. Catal. B Environ. Energy*, 2025, **375**, 125418.

[23] W. Wang, Z. Chen, C. Li, B. Cheng, K. Yang, S. Zhang, G. Luo, J. Yu, S. Cao, *Adv. Funct. Mater.*, 2025, **35**, 2422307.

[24] X. Zhai, Z. Wei, Z. Lu, X. Zhang, X. Chen, Y. Liu, J. Deng, Y. Zhu, H. Dai, L. Jing, *Adv. Funct. Mater.*, 2025, **35**, 2503667.

[25] K. Zhang, M. Dan, J. Yang, F. Wu, L. Wang, H. Tang, Z. Q. Liu, *Adv. Funct. Mater.*, 2023, **33**, 2302964.

[26] X. Xia, J. Feng, Z. Zhong, X. Yang, N. Li, D. Chen, Y. Li, Q. Xu, J. Lu, *Adv. Funct. Mater.*, 2024, **34**, 2311987.

[27] S. Zhi, X. Zou, C. Yang, D. Wu, H. Guo, *Appl. Catal. B Environ. Energy*, 2025, **371**, 125215.

[28] S. Yan, Y. Li, X. Yang, X. Jia, J. Xu, H. Song, *Adv. Mater.*, 2024, **36**, 2307967.

[29] J. Hu, B. Li, X. Li, T. Yang, X. Yang, J. Qu, Y. Cai, H. Yang, Z. Lin, *Adv. Mater.*, 2024, **36**, 2412070.

[30] H. He, Z. Wang, J. Zhang, C. Shao, K. Dai, K. Fan, *Adv. Funct. Mater.*, 2024, **34**, 2315426.

[31] D. Jiao, C. Ding, M. Xu, X. Ruan, S. K. Ravi, X. Cui, *Adv. Funct. Mater.*, 2024, **34**, 2416753.

[32] T. Tian, Q. Shen, Y. Yuan, J. Wang, X. Yang, D. Jiang, C. Zhu, G. Xu, Y. Yuan, *Appl. Catal. B Environ. Energy*, 2025, **378**, 125567.

[33] Y. Wang, X. Zhao, G. Han, J. Bi, Y. Zhao, *Adv. Funct. Mater.*, 2025, **35**, 2508550.